1   **Revision 1**

2   **High-pressure phase transitions in $FeCr_2O_4$ and structure analysis of new post-spinel $FeCr_2O_4$ and**

3   **$Fe_2Cr_2O_5$ phases with meteoritical and petrological implications**

4

5   **Takayuki Ishii[1], Hiroshi Kojitani[1], Shoichi Tsukamoto[1], Kiyoshi Fujino[2], Daisuke Mori[1], Yoshiyuki**

6   **Inaguma[1], Noriyoshi Tsujino[3], Takashi Yoshino[3], Daisuke Yamazaki[3], Yuji Higo[4], Kenichi Funakoshi[4] and**

7   **Masaki Akaogi[1]**

8   [1]Department of Chemistry, Gakushuin University, Mejiro, Toshima-ku, Tokyo 171-8588, Japan

9   [2]Geodynamics Research Center, Ehime University, Matsuyama, Ehime 790-8577, Japan

10   [3]Institute for Study of the Earth's Interior, Okayama University, Misasa, Tottori 682-0193, Japan

11   [4]Japan Synchrotron Radiation Research Institute, Koto, Hyogo 679-5198, Japan

12

13   **Abstract**

14   We determined phase relations in $FeCr_2O_4$ at 12-28 GPa and 800-1600ºC using a multianvil apparatus. At

15   12-16 GPa, $FeCr_2O_4$ spinel (chromite) first dissociates into two phases: a new $Fe_2Cr_2O_5$ phase + Cr_2O_3 with the

16   corundum structure. At 17-18 GPa, the two phases combine into $CaFe_2O_4$-type and $CaTi_2O_4$-type $FeCr_2O_4$

17   below and above 1300ºC, respectively. Structure refinements using synchrotron X-ray powder diffraction data

18   confirmed the $CaTi_2O_4$-structured $FeCr_2O_4$ (*Cmcm*), and indicated that the $Fe_2Cr_2O_5$ phase is isostructural to a

19   modified ludwigite-type $Mg_2Al_2O_5$ (*Pbam*). *In situ* high-pressure high-temperature X-ray diffraction

20   experiments showed that $CaFe_2O_4$-type $FeCr_2O_4$ is unquenchable and is converted into another $FeCr_2O_4$ phase

21   on decompression. Structural analysis based on synchrotron X-ray powder diffraction data with transmission

22   electron microscopic observation clarified that the recovered $FeCr_2O_4$ phase has a new structure related to

23   $CaFe_2O_4$-type. The high-pressure phase relations in $FeCr_2O_4$ reveal that natural $FeCr_2O_4$-rich phases of

24   $CaFe_2O_4$- and $CaTi_2O_4$-type structures found in the shocked Suizhou meteorite were formed above about 18

25   GPa at temperature below and above 1300 $^{\circ}$C, respectively. The phase relations also suggest that the natural

26   chromitites in the Luobusa ophiolite previously interpreted as formed in the deep-mantle were formed at

27   pressure below 12-16 GPa.

28   **Keywords:** Post-spinel, Rietveld analysis, crystal structure, high pressure, phase transition, shocked meteorite,

29   $FeCr_2O_4$, ophiolite

30

31

2

Introduction

32

33   High-pressure transitions of spinel-structured $A^{2+}B^{3+}_2O_4$ compounds, "post-spinel transitions", have been

34   paid much attention because of their geophysical significance including investigation on dense aluminous

35   phases in the subducted crust into the deep mantle. $CaFe_2O_4$-, $CaTi_2O_4$- and $CaMn_2O_4$-structures have been

36   regarded as the $A^{2+}B^{3+}_2O_4$ post-spinel structures (Ringwood, 1975). We hereafter abbreviate $CaFe_2O_4$, $CaTi_2O_4$

37   and $CaMn_2O_4$ as CF, CT and CM respectively. The $A^{2+}B^{3+}_2O_4$ phases with the CF- and CT-structures (space

38   groups *Pnma* and *Cmcm*, respectively) consist of double chains of edge-shared $B^{3+}O_6$ octahedra running

39   parallel to one of the orthorhombic cell axes, and A^{2+} ions occupy tunnel spaces surrounded by corner-sharing

40   of four double chains (Decker et al., 1957; Rogge et al., 1998; Yamanaka et al., 2008). The CM-structure

41   (*Pbcm*) is interpreted to be formed by Jahn-Teller distortion of $B^{3+}O_6$ octahedra from the CT-structure (Geisber

42   et al., 2001; Yamanaka et al., 2008). $FeCr_2O_4$ chromite with the spinel structure forms spinel solid solutions

43   with other end-members, $MgCr_2O_4$, $MgAl_2O_4$, $FeAl_2O_4$ etc., in various crustal and upper-mantle rocks.

44   Chromite is also a major chromium ore mineral. It was recently found that by compression at room temperature

45   pure $FeCr_2O_4$ spinel undergoes a cubic-to-tetragonal transition due to Jahn-Teller effect in tetrahedrally

46   coordinated Fe^{2+} (Kyono et al., 2012). However, compared with other $A^{2+}B^{3+}_2O_4$ spinels, particularly $MgAl_2O_4$,

47   little is known about high-pressure transitions in $FeCr_2O_4$.

48          $FeCr_2O_4$-rich spinel and its high-pressure polymorphs were found in a shock-metamorphosed L6-chondrite

49   named Suizhou which contained shock-induced melt veins and high-pressure minerals including ringwoodite

50   and majorite garnet (Chen et al., 2003a, b). Chen et al. (2003a, b) synthesized CF- and CT-structured chromite

51   phases with the same composition as in the L6-chondrite in laser-heated diamond anvil cell experiments at 12.5

52   GPa and above 20 GPa, respectively. They interpreted that the $FeCr_2O_4$-rich high-pressure polymorphs in the

53   meteorite were the CF- and CT-phases, on the basis of powder X-ray diffraction patterns. However, detailed

54   structural analysis of the CF- and CT-phases and determination of their stability relations with chromite spinel

55   have not yet been made. Chromitites composed mostly of $FeCr_2O_4$-rich spinel which occured in the Luobusa

56   ophiolite in Tibet included high-pressure minerals such as diamond and coesite, which suggest possible

57   deep-mantle origin of the chromitites (Yang et al., 2007; Arai, 2010; Yamamoto et al., 2009).

58   At 1600 ^{o}C, $MgAl_2O_4$ spinel transforms to a mixture of $MgO + Al_2O_3$ at 16 GPa and to a CF-type

59   phase at 27 GPa (Akaogi et al., 1999). The CF-type $MgAl_2O_4$ transforms to a CT-type phase at about 40 GPa

60   (Funamori et al., 1998). Above about 2000ºC, however, we recently found that $MgAl_2O_4$ spinel first dissociates

61   into an $Mg_2Al_2O_5$ phase $+ Al_2O_3$ at 20-22 GPa, and changes to CF phase at 26-28 GPa via an unknown

62    $MgAl_2O_4$ phase (Kojitani et al. 2010). Our structure analysis indicated that the $Mg_2Al_2O_5$ phase has a modified

63   ludwigite structure (*Pbam*) consisting of edge- and corner-shared $(Mg,Al)O_6$ octahedra running parallel to

64   c-axis, and tunnel spaces surrounded by the octahedra are occupied by Mg^{2+} (Enomoto et al., 2009). We

65   abbreviate the modified ludwigite structure as mLd. The mLd structure of $Mg_2Al_2O_5$ is similar to that of

66   recently found high-pressure Fe_4O_5 phase (Lavina et al., 2011), but the manner of octahedral connection is

67   different between the two structures. To our best knowledge, the $Mg_2Al_2O_5$ phase has been the only compound

68   having the mLd structure.

69   In this study, we have investigated in detail the post-spinel transitions of $FeCr_2O_4$ chromite at high

70   pressure and high temperature. We have found that with increasing pressure $FeCr_2O_4$ chromite first dissociates

71   into a mixture of $Fe_2Cr_2O_5$ and Cr_2O_3. The two phases combine into a $FeCr_2O_4$ phase with the CF structure at

4

72 relatively low temperature and into the CT-type $FeCr_2O_4$ at relatively high temperature. We have also found by

73 *in situ* X-ray diffraction experiments that the CF-type $FeCr_2O_4$ is changed into a $FeCr_2O_4$ phase with a new

74 CF-related structure on release of pressure. The high-pressure phase relations in $FeCr_2O_4$ involving these new

75 phases have been precisely determined. The structures of the $Fe_2Cr_2O_5$ phase and the CF-related structured

76 $FeCr_2O_4$ phase have been analyzed and refined, together with that of CT-type $FeCr_2O_4$. Based on the data, we

77 discuss on P,T conditions of the shock event which the Suizhou meteorite suffered and on the origin of the

78 chromitites in the Luobusa ophiolite in the deep mantle.

79

Experimental methods

81 1. Starting materials

82      $FeCr_2O_4$ spinel was prepared from a mixture of reagent-grade Fe_2O_3 and Cr_2O_3 with 1:2 molar ratio.

83 The mixture was heated at 1200ºC for 24 h in a controlled oxygen fugacity using a mixture of H_2, CO_2 and Ar

84 with volume ratios of 1:1:2. After heating, the product was confirmed to be single-phase of $FeCr_2O_4$ with spinel

85 structure by a powder X-ray diffractometer (CrKα) and a scanning electron microscope with an energy

86 dispersive X-ray spectrometer (SEM-EDS). The $FeCr_2O_4$ spinel powder mixed with 5 wt% Fe metal powder

87 was used as the starting material for phase equilibrium experiments. Fe_xO wüstite was made by heating a

88 reagent-grade Fe_2O_3 at the same conditions as $FeCr_2O_4$ spinel. The composition of Fe_xO was estimated as x =

89 0.933 from the relationship between the lattice parameter and x by McCammon (1993). The $Fe_{0.933}O$ and Cr_2O_3

90 powders were mixed with atomic ratio Fe : Cr = 1:1 with additional 5 wt% Fe metal powder, and the mixture

91 was used as the starting material to synthesize $Fe_2Cr_2O_5$ phase. The addition of 5 wt% Fe metal in both the

5

92   starting materials was to keep iron in the phases ferrous state.

93

94   2. High-pressure high-temperature experiments by quench method

95   The high-pressure high-temperature quench experiments were carried out at 11.7-28 GPa and

96   800-1600ºC with a Kawai-type 6-8 multianvil high-pressure apparatus at Gakushuin University. Tungsten

97   carbide anvils with truncated edge lengths (TEL) of 2.5 mm were used with a pressure medium of Cr_2O_3-doped

98   MgO octahedron with 7.0 mm edge length. A cylindrical rhenium furnace was placed in the center of the

99   magnesia octahedron. For thermal insulation, a $LaCrO_3$ sleeve was put outside of the rhenium heater and

00    $LaCrO_3$ end-plugs were placed at both ends of the heater. Temperature was measured at the central part of

01   outer-surface of the furnace with a Pt/Pt-13%Rh thermocouple of 0.1 mm in diameter. No correction was made

02   on pressure effect of the thermocouple emf. Phase relations of $FeCr_2O_4$ were examined with the multi-sample

03   cell technique (Fei and Bertka, 1997) described by Ishii et al. (2011, 2012). The starting material of $FeCr_2O_4$

04   spinel + 5 wt% Fe and a pressure marker (Mg_2SiO_4, $MgSiO_3$ or $MgO+Al_2O_3$) were packed in two holes of 0.2

05   mm diameter in a Re capsule which was 1.0 mm in diameter and 0.7 mm in thickness. Two Re discs of 1.0 mm

06   in diameter and 0.1 mm thickness were placed on both sides of the Re capsule. A boron nitride sleeve and discs

07   were inserted between the Re capsule and the heater for electrical insulation.

08   The $FeCr_2O_4$ high-pressure phases with the CF-related and CT structures used for Rietveld refinements

09   were synthesized from $FeCr_2O_4$ spinel as the starting material at 25 GPa, 1000ºC with a Fe capsule and at 25

10   GPa, 1400ºC with an Au-Pd capsule, respectively. A BN sleeve was placed between the Fe or Au-Pd capsule

11   and the tubular rhenium heater for electrical insulation. The CF-related $FeCr_2O_4$ phase for TEM observation

6

12   and the $Fe_2Cr_2O_5$ high-pressure phase for structure refinement were synthesized from sample materials packed

13   directly in the rhenium heater and held at 25 GPa, 1000ºC and 16 GPa, 1300ºC, respectively.

14   Pressure calibration was made in a similar manner to those of Ishii et al. (2011, 2012). The pressure

15   was calibrated at room temperature using transition points of ZnS (15.5 GPa), GaAs (18.3 GPa) and GaP (23

16   GPa) (Dunn and Bundy, 1978, Ito, 2007). Temperature effect on pressure was corrected at 1600°C by Mg_2SiO_4

17   forsterite-wadsleyite transition (15.1 GPa) (Morishima et al., 1994), Mg_2SiO_4 wadsleyite-ringwoodite transition

18   (21.3 GPa) (Suzuki et al., 2000), $MgSiO_3$ akimotoite-perovskite transition (22.3 GPa) (Fei et al., 2004), and

19   transition of Al_2O_3 corundum + MgO periclase to $MgAl_2O_4$ calcium ferrite (24.9 GPa) (Irifune et al., 2002),

20   using the pressure markers ($MgSiO_3$, Mg_2SiO_4 and MgO + Al_2O_3) packed in one of the holes of the Re capsule.

21   The pressure calibration curve at 1200 ^oC was very close to that at 1600°C. The relative uncertainty of pressure

22   of the quench experiments in this study was estimated to be about ±0.2 GPa (Ishii et al., 2011, 2012).

23   In each high-pressure run, pressure was increased to a targeted pressure at an almost constant rate

24   during about 2-4 h, and then temperature was increased to 800-1600°C at a rate of about 100°C/min. The

25   sample assembly was kept for 1-3 h at the pressure-temperature conditions, then quenched, and decompressed

26   for 5-12 h, and finally recovered to ambient conditions. The recovered samples in the capsules were mounted

27   on slide-glass plates with epoxy resin, and were polished into flat for phase identification and compositional

28   analysis.

29   The phases in the recovered samples were identified using a microfocus X-ray diffractometer (Rigaku

30   RINT 2500V, MDG) with an X-ray beam collimated to 50 μm. The powder X-ray diffractometer (Rigaku

31   RINT 2500V) was used with the step-scan mode (step size of 0.02º) in the 2θ range of 10-140º to determine

7

32   lattice parameters of the samples. Both the X-ray diffraction measurements were conducted using CrKα

33   radiated from a rotating anode at 45 kV and 250 mA. The scanning electron microscope (SEM, JEOL

34   JMS-6360) with the energy dispersive X-ray spectrometer (EDS, Oxford INCA energy 300) was used for

35   composition analysis and also for phase identification in the recovered samples. The SEM was operated with

36   acceleration voltage of 15 kV and probe current of 0.43 nA. Natural fayalite and synthetic Cr_2O_3 eskolaite were

37   used as standard materials for Fe and Cr, respectively.

38

39   3.   *In-situ* X-ray observations at high pressures and high temperatures

40   High-pressure high-temperature *in-situ* X-ray observations were conducted using a high-pressure

41   apparatus SPEED-1500 with a Kawai-type multianvil system with intense white X-ray of synchrotron radiation

42   at the beam line BL04B1 at SPring-8. An X-ray beam collimated to 50 × 150 μm was emitted to the sample

43   chamber in the pressure medium via horizontal and vertical slits through the anvil gap of the first and

44   second-stage anvils. Energy dispersive X-ray diffraction was measured in the range between 3 and 150 keV

45   with a pure Ge solid-state detector connected to a multichannel analyzer with 4096 channels, and radiographic

46   images of the sample chamber were recorded using a CCD camera. The detector was calibrated using known

47   X-ray emission lines of a set of metals (Au, Cu, Mo, Ag, Ta, Pt and Pb). The diffraction angle (2θ) was fixed to

48   about ~6º using diffraction peaks of MgO at ambient conditions. We used sintered MgO as the pressure maker,

49   and pressure was estimated on the basis of equation of state of MgO by Speziale et al. (2001).

50   The mixture of $FeCr_2O_4$ spinel + 5 wt% Fe was used as the starting material for the *in-situ*

51   high-pressure high-temperature experiments. Tungsten carbide anvils with 4 mm TEL were used in

8

52   combination with a Cr_2O_3-doped MgO octahedron of 10.0 mm edge length as the pressure medium. A

53   cylindrical TiB_2-BN was put in the central part of the magnesia octahedron as a heating element. A $LaCrO_3$

54   sleeve and end-plugs were placed between the heater and the pressure medium. Mo electrodes were inserted in

55   the center of both the $LaCrO_3$ end-plugs. Temperature was measured in the central part of the furnace with a

56   W-3%Re/W-25%Re thermocouple of 0.05 mm in diameter. The pressure effect of the thermocouple emf was

57   ignored. The MgO pressure maker was put next to the thermocouple junction on both sides, and the samples

58   were put between the pressure marker and MgO end-plugs. Mo foils were put at both ends of the sample. The

59   graphite and MgO rods were placed in the pressure medium and the $LaCrO_3$ sleeve as a window for the X-ray

60   beam.

61   The press load was raised to the desired values up to 1000 ton, and then temperature was gradually

62   increased to 1000°C in about 30 min. The samples were kept at the targeted temperature for 1 h. The diffraction

63   patterns of the sample and the pressure marker were measured for 120 and 300 sec, respectively. Using the

64   diffraction patterns at high pressures and room temperature, lattice parameters of CF-type $FeCr_2O_4$ were refined

65   by Le Bail method (Le Bail, 1988) using the GSAS-EXPGUI software package (Larson and Von Dreele, 2000;

66   Toby, 2001; Sanehira et al., 2008). Reduced Chi-square (χ^2) and R_P values (Larson and Von Dreele, 2000)

67   estimated by Le Bail fitting were used to evaluate goodness of fit after the refinement. χ^2 values were converged

68   less than ~3, suggesting that the fits were of high quality.

69

70   4. Transmission electron microscopic observations and Rietveld structure analyses

71   Transmission electron microscopic (TEM) observation of CF-related $FeCr_2O_4$ phase was performed to

9

72   constrain its space group and to determine approximate cell parameters. For the TEM observation, a small chip

73   of ~0.1 μm thickness was prepared from the central part of the sintered sample synthesized at 25 GPa and

74   1000°C. The thin film was observed by the TEM (JEOL, JEM-2010) using an accelerating voltage 200 kV at

75   Geodynamics Research Center, Ehime University. To examine possible existence of centrosymmetry of the

76    $FeCr_2O_4$ phase, the optical second harmonic generation (SHG) response was measured with a Continuum

77   Minilite YAG:Nd laser (λ=1064 nm) (Rabin and Tang, 1975, Inaguma et al., 2012).

78   For structural determination and refinement, angle-dispersive synchrotron powder X-ray diffraction

79   measurements of CF-related and CT-type $FeCr_2O_4$ phases and the mLd-type $Fe_2Cr_2O_5$ phase were conducted

80   using an imaging plate as the detector and a Debye-Scherrer camera in a 2θ angle of 0-75º with an angle

81   resolution of 0.01º in the beam line BL02B2 at SPring-8. The wavelength of the X-ray was determined using

82   fluorite-type CeO_2 as 0.41927 Å for CT-type $FeCr_2O_4$ and $Fe_2Cr_2O_5$ and as 0.49973 Å for CF-related $FeCr_2O_4$.

83   Each polycrystalline sample was finely ground in an agate mortar, and was packed in a Lindemann glass

84   capillary. The X-ray diffraction patterns were measured at ambient conditions on rotating the samples along the

85   capillary axis.

86   Rietveld analysis was performed using the RIETAN-FP/VENUS package (Izumi and Momma, 2007).

87   The initial structure models of CT-type $FeCr_2O_4$ and mLd-type $Fe_2Cr_2O_5$ were $CaTi_2O_4$ (Bertaut and Blum,

88   1956) and $Mg_2Al_2O_5$ (Enomoto et al., 2009), respectively. The starting structure model of CF-related $FeCr_2O_4$

89   was constructed by the powder charge-flipping method using SUPERFLIP and EDMA softwares (Baerlocher et

90   al., 2007, Palatinus et al., 2007, 2012). Observed integrated intensities of synchrotron XRD pattern (λ =

91   0.49973 Å), $|F_{obs}|^2$, were extracted by the Le Bail analysis method (Le Bail, 1988). The initial values of lattice

10

92   parameters in the Rietveld refinement of each sample were determined from the powder X-ray diffraction

93   patterns (CrKα) with DICVOL06 software (Loüer and Boultif, 2007). Corundum-type Cr_2O_3 was included as

94   the second phase in the Rietveld analysis of all the samples, and Re metal as the third phase in the analysis of

95   mLd-type $Fe_2Cr_2O_5$.

96

97   **Results and discussion**

98   1.   High-pressure phase transitions in $FeCr_2O_4$ by quench and *in situ* X-ray diffraction experiments.

99   Table 1 summarizes the results of the quench experiments in $FeCr_2O_4$ that indicate phases in the

00   recovered run products identified by microfocus and powder X-ray diffractometers and SEM-EDS. At

01   800-1600 ^oC and about 12-16 GPa, $FeCr_2O_4$ spinel first dissociates into a mixture of two phases. Powder X-ray

02   diffraction patterns of the dissociation products consisted of corundum-type Cr_2O_3 and another phase whose

03   diffraction pattern was very similar to that of mLd-type $Mg_2Al_2O_5$ (Enomoto et al., 2009). The SEM-EDS

04   analysis indicated that the former phase had Cr_2O_3 composition and the latter $Fe_2Cr_2O_5$ with analyzed Fe : Cr

05   ratio of 1.98(1) : 2.01(2). As described below, the structural refinement confirmed that the $Fe_2Cr_2O_5$ phase has

06   the mLd structure. At temperature above 1300-1400 ^oC at 16-18 GPa, the mixture of mLd-type $Fe_2Cr_2O_5$ and

07   corundum-type Cr_2O_3 combine into a single phase whose diffraction pattern was very similar to that of $CaTi_2O_4$.

08   The Rietveld refinement and SEM-EDS analysis confirmed that the phase has the CT structure with $FeCr_2O_4$

09   composition (Fe : Cr = 0.99(1) : 2.01(1)), as shown below. At 16-18 GPa below 1300-1400 ^oC, on the other

10   hand, the mixture of $Fe_2Cr_2O_5$ and Cr_2O_3 changes into another phase with the composition of $FeCr_2O_4$ (Fe : Cr

11   = 0.99(1) : 2.00(1)). Figure 1 shows that, though the diffraction pattern of this phase resembles that of the

11

12   CF-type structure, relative intensities of some diffraction lines are very different from those of the simulated

13   pattern for CF-type $FeCr_2O_4$. The structural analysis described below clarified that this recovered $FeCr_2O_4$

14   phase has a different from the CF-type structure but related to it. Therefore, we call it a "modified

15    $CaFe_2O_4$-type" (mCF) $FeCr_2O_4$ phase. Although detailed results of structure analyses of CT-type $FeCr_2O_4$,

16   mCF-type $FeCr_2O_4$ and mLd-type $Fe_2Cr_2O_5$ are described in the following section, we use here lattice

17   parameters determined by the structure analyses and densities of the phases listed in Table 2. Figure 2 illustrates

18   the phase relations in $FeCr_2O_4$ up to 28 GPa and 1600°C. The densities of $FeCr_2O_4$ spinel (Lenaz et al., 2004),

19    $Fe_2Cr_2O_5$ mLd + Cr_2O_3 corundum (Belokoneva and Shcherbakova, 2003), $FeCr_2O_4$ mCF, and $FeCr_2O_4$ CT are

20   5.059(1), 5.48(4), 5.213(1), and 5.604(1) g/cm^3, respectively, at ambient conditions. The lower density of

21   mCF-type $FeCr_2O_4$ compared to that of mLd-type $Fe_2Cr_2O_5$ + Cr_2O_3 corundum is inconsistent with the fact that

22   mCF was synthesized at higher pressure than mLd + Cr_2O_3. This strongly suggests that mCF is not the stable

23   phase at the P,T conditions of our experiments but is a retrograde transformation product. Therefore, we

24   conducted in situ X-ray diffraction experiments in the P,T field from which mCF was recovered.

25   Figure 3 shows *in-situ* X-ray diffraction patterns of $FeCr_2O_4$ at high pressures and high temperatures.

26   By pressurization to 26.2 GPa at room temperature, diffraction pattern of $FeCr_2O_4$ cubic spinel + α-Fe (I in Fig.

27   3a) changed into a broad diffraction pattern consisting of tetragonal spinel, cubic spinel and ε-Fe (II in Fig. 3a).

28   The cubic-tetragonal transition of $FeCr_2O_4$ spinel at room temperature is consistent with the results by Kyono et

29   al. (2012). By heating to 1000 °C at 26.2 GPa, the diffraction pattern of $FeCr_2O_4$ transformed into a different

30   one (III) with a small pressure decrease to 22.7 GPa. After quenching, the diffraction patterns collected in

31   decompression at 20.1 GPa (IV), at 16.5 GPa (V) and down to at least 9.3 GPa are consistent with (III). It

12

32   should be noted that peaks of ε-Fe changed into those of γ-FeH$_x$ + FeO by heating to 1000 ^{o}C, probably due to

33   reaction of Fe with H$_2$O adsorbed in the sample, as reported by Ohtani et al. (2005). To examine these patterns

34   in more detail, we simulated diffraction pattern at 16.5 GPa and 27ºC for CF-type FeCr$_2$O$_4$ and compared it

35   with the observed one at the P, T conditions in Figure 3b. Except for the peaks of γ-FeH$_x$ and FeO, the observed

36   diffraction pattern is quite consistent with the simulated pattern of CF-type FeCr$_2$O$_4$. After decompression to

37   ambient conditions (VI in Fig. 3a), however, the diffraction pattern was changed to that of mCF-type. These *in*

38   *situ* X-ray diffraction profiles indicate that the stable phase is not mCF but the CF phase at the relevant P, T

39   conditions and that CF changes to mCF by decompression.

40   We determined the cell volumes of CF-type FeCr$_2$O$_4$, 248.44(3) and 245.16(2) Å^3, at 16.5 and 20.1

41   GPa, respectively, at 25 ^{o}C by in situ X-ray diffraction measurements, and those per formula unit are shown in

42   Figure 3c. By fitting the third-order Birth-Murnaghan equation of state (BM) to the cell volume data, assuming

43    $K' = 4$, bulk modulus (K_0) and zero-pressure volume (V_0) were determined to be 199 GPa and 266.95 Å^3,

44   respectively, in which the latter gives molar volume (V_m) of 40.19 cm^3/mol. The obtained K_0 and V_m are

45   consistent with an empirical relationship, K_0V_m = constant, for CF-type oxides, when we compare our K_0 and

46   V_m of CF-type FeCr$_2$O$_4$ with those of other CF-type oxides, MgAl$_2$O$_4$ (213 GPa and 36.22 cm^3/mol) by Irifune

47   et al. (2002) and NaAlSiO$_4$ (220 GPa and 36.58 cm^3/mol) by Dubrovinsky et al. (2002). The V_0 of CF phase is

48   smaller by about 7 % than that of mCF, smaller by ~5 % than zero-pressure volume of Fe$_2$Cr$_2$O$_5$ mLd + Cr$_2$O$_3$

49   corundum, and very close to that of CT-type FeCr$_2$O$_4$. As shown in Fig. 2, CF-type FeCr$_2$O$_4$ transforms to CT at

50   27.5 GPa at 1300 ^{o}C. The slightly smaller V_0 of CF than CT is probably derived from relatively large

51   uncertainties in the K_0 and V_0 of CF determined using only the two volume data. As a future study, it is

52   necessary to measure more precise compression data of CF. Based on all the results on mCF and CF, we

53   conclude that CF phase is stable above about 18-19 GPa below about 1300 $^{\circ}$C, and the CF phase is converted to

54   mCF phase on release of pressure.

55   In Fig. 2, phase boundaries between $FeCr_2O_4$ spinel and mLd-type $Fe_2Cr_2O_5$ + Cr_2O_3 and between

56   mLd-type $Fe_2Cr_2O_5$ + Cr_2O_3 and CT-type $FeCr_2O_4$ have small negative slopes. While the boundary between

57   mLd-type $Fe_2Cr_2O_5$ + Cr_2O_3 and CF-type $FeCr_2O_4$ has a small positive slope, that between CF-type and

58   CT-type has a strongly negative slope probably due to the small volume difference. The high-pressure phase

59   transition behaviors of $FeCr_2O_4$ shown here have some similarities to those in $MgAl_2O_4$ by Enomoto et al.

60   (2009) and Kojitani et al. (2010).

61   Chen et al. (2003b) reported that CF-type and CT-type phases were recovered after compression of natural

62    $FeCr_2O_4$-rich spinels to maximum pressures of 12.5 GPa and 20 GPa, respectively, at about 2000 $^{\circ}$C. These

63   results exhibit some inconsistency with our study with respect to the P,T conditions of CF-type $FeCr_2O_4$. The

64   differences in synthesis pressure and temperature for CF phase may be due to uncounted thermal pressure

65   produced during laser-heating (in fact they measured pressure only before laser-heating). Minor components

66   other than $FeCr_2O_4$ may also affect stability fields of the CF-type and CT-type phases.

67

68   2. Crystal structures of modified $CaFe_2O_4$(mCF)-type $FeCr_2O_4$, $CaTi_2O_4$(CT)-type $FeCr_2O_4$, and modified

69   ludwigite(mLd)-type $Fe_2Cr_2O_5$.

70   Electron diffraction patterns of mCF by TEM are shown in Figure 4. The results of Rietveld analysis using

71   synchrotron X-ray diffraction pattern of mCF, CT and mLd are shown in Figures 5-8 with the data in Tables 3

14

72   and 4. The crystal structures illustrated in Figures 5-8 were drawn by VESTA (Momma and Izumi, 2008). The

73   structural parameters and reliability factors (R_{wp}, R_B and R_F) and goodness-of-fit indicator (S) of mCF, CT and

74   mLd are shown in Table 3. We confirmed that R_{wp}, R_B, R_F and S for the mCF, CT and mLd and the impurity

75   phase converged to sufficiently small values. The interatomic distances, bond angles, effective coordination

76   numbers (n_c) (Nespolo et al., 2001) and the bond valence sum (BVS) (Brown and Altermatt, 1985) values of

77   mCF, CT and mLd are shown in Table 4. In the following sections, we describe detailed results on structure

78   analyses of the three phases.

79

80   a) mCF-type $FeCr_2O_4$

81   As shown in Figures 1 and 3, the powder X-ray diffraction pattern of $FeCr_2O_4$ mCF is similar to CF. But

82   the intensity of that is different from CF. To determine the crystal structure of $FeCr_2O_4$ mCF, we first examined

83   the mCF sample by TEM. The synthesized sample, run no. 40, was used for TEM observation. Figure 4

84   illustrates electron diffraction patterns ((a) $hk0$ plane, (b) $h0l$ plane and (c) $0kl$ plane) taken from different

85   grains of the sample. In Figure 4a, diffraction spots of $hk0$ with $h = 2n + 1$ had weaker intensities than those

86   with $h = 2n$, and the spots disappeared by declining the $hk0$ plane from the Bragg condition. Therefore, the

87   spots of $hk0$ with $h = 2n + 1$ appeared by double diffractions from $hk1$ plane, showing the extinction rule of $h =$

88    $2n$. The spots of $0k0$ with $k = 2n + 1$ were also double diffractions in $hk0$ plane, because they vanished by

89   declining the $hk0$ plane. In a similar manner, Figure 4c shows the systematic absence of $k + l = 2n + 1$ in the

90   spots $0kl$, respectively. No extinction rule was observed in Figure 4b except for $h00$ with $h = 2n +1$ and $00l$ with

91    $l = 2n +1$, which appeared by double diffractions in $h0l$ plane. The reflection conditions derived from TEM

15

92   observation are consistent with those of X-ray diffraction. From these results of TEM observations, we

93   conclude that mCF-type $FeCr_2O_4$ has an orthorhombic unit cell with space group *Pnma* or *Pn2₁a*. Next, we

94   performed the SHG measurement, but no SHG signal was observed for the run no. 40 sample. This indicated

95   that the structure of mCF has centrosymmetry and thus its space group is limited to *Pnma*.

96   The lattice parameters of mCF were obtained as the initial values for Rietveld refinement, using 33

97   reflections of the powder X-ray diffraction pattern (CrKα) with DICVOL06. Figure 5a shows synchrotron

98   powder X-ray diffraction patterns of *m*CF. $|F_{obs}|^2$ values of 210 reflections in the region d > 0.95 Å were

99   extracted by the Le Bail method. We used the powder charge flipping method to obtain the initial structure of

00   mCF. The cation positions (Fe and Cr) determined using EDMA software were close to those in the CF-type

01   structure, while the oxygen positions could not be determined because oxygen has relatively low electron

02   number. Therefore, we performed Rietveld refinement from the initial structure model in which oxygens were

03   at the same positions as those of CF-type $CaCr_2O_4$ (Arévalo-López et al. 2010) and Fe and Cr at the positions

04   determined by EDMA.

05   The results of Rietveld analysis of mCF in Figures 5a and 6 indicate mCF has edge-shared CrO_6

06   octahedral chains running along b-axis, and the two octahedral chains form double chains by edge-sharing.

07   Furthermore, by sharing corners of these four double chains, tunnel structure is formed. Although the structure

08   of mCF is very similar to CF-type structure, positions of Fe are moved by about half of b-edge length along the

09   b-axis of CF, while Cr and O positions in mCF are almost the same as in the CF structure. Thus, the

10   coordination polyhedron of Fe in mCF is FeO_5 (FeO_3 plane triangle + two oxygens), while that in CF is FeO_8

11   bicapped trigonal prism (FeO_6 prism + two oxygens). A similar asymmetric coordination environment of Fe to

16

12   that of mCF is found in the structure of $Fe_3(PO_4)_2$ ($P2_1/c$) (Kosiner and Rea, 1974). The reason why Fe^{2+} ions

13   prefer such the special coordination in the mCF structure may be the relatively small ionic radius of $^{VIII}Fe^{2+}$

14   (0.91 Å), compared with those of A^{2+} in other CF-structured phases such as $CaCr_2O_4$ and $CdCr_2O_4$ (^{VIII}Ca: 1.12

15   Å, ^{VIII}Cd: 1.10 Å) in the tunnels formed by CrO_6 double-octahedral chains (Shannon, 1976; Hill et al., 1956;

16   Arévalo-López et al. 2010).

17

18   (b) CT-type $FeCr_2O_4$

19   Figures 5b and 7 show, together with Tables 3 and 4, the results of Rietveld refinement using

20   synchrotron X-ray diffraction pattern of CT-type $FeCr_2O_4$. Although the double chains of mCF are linked to

21   have a glide plane corresponding to the plane and direction of corner-sharing between the octahedra, those of

22   CT are linked to have a mirror plane in the direction of those, indicating that both the structures have different

23   types of tunnels. The coordination number of Fe in the tunnel of CT is 6 + 2 (bicapped trigonal prism).   We

24   compared CT-type $FeCr_2O_4$ with the structure of $CaTi_2O_4$ (Bertaut and Blum, 1956). The Cr-O distances in the

25   CrO_6 octahedron are 1.96-2.03 Å, with the average distance, 1.997 Å, which is close to 2.015 Å by summation

26   of effective ionic radii of Cr^{3+} (0.615 Å for six-fold coordination) and O^{2-} (1.40 Å) (Shannon, 1976). The bond

27   angles of O1-Cr1-O3 and O2-Cr1-O3 are 171.3º and 178.7º, respectively, and those of O1-Ti1-O3 and

28   O2-Ti1-O3 of $CaTi_2O_4$ are 171.2º and 166.2º, respectively. Therefore, bond angles (124.1º of Cr1-O2-Cr1 and

29   141.6º of Ti1-O2-Ti1) of two corner-shared double chains are largely different. This may depend on the sizes of

30   ion radii of A-site cations (Fe^{2+} and Ca^{2+}). The effective coordination number (n_c) (Nespolo et al., 2001) of Fe

31   was calculated to be 4.87, and that of Ca in $CaTi_2O_4$ 6.86. The Fe-O distances in the FeO_8 bicapped trigonal

17

32   prism are 2.01-2.31 Å (FeO$_6$ prism) and 2.66 Å (two longest Fe-O bonds), but the Ca-O distances in the CaO$_8$

33   bicapped trigonal prism of CaTi$_2$O$_4$ are 2.32-2.46 Å (CaO$_6$ prism) and 2.74 Å (two longest Ca-O bonds). Two

34   longest Fe-O bonds are too long, compared with summation of effective ion radii Fe^{2+} (0.92 Å for eight-fold

35   coordination) and O^{2-} (1.40 Å) (Shannon, 1976). This indicates the coordination number of Fe in tunnel spaces

36   is 6 rather than 8.

37

38   (c) mLd-type Fe$_2$Cr$_2$O$_5$.

39   Figures 5c and 8 show the results of Rietveld analysis using synchrotron X-ray diffraction pattern of

40   mLd-type Fe$_2$Cr$_2$O$_5$, together with Tables 3 and 4. The isotropic atomic displacement parameters of oxygens of

41   mLd-type Fe$_2$Cr$_2$O$_5$ were fixed to the same value as done in CT-type FeCr$_2$O$_4$. The site occupancies of Fe and

42   Cr in mLd-type Fe$_2$Cr$_2$O$_5$ were estimated from bond distances between cations and oxygens. The crystal

43   structure of mLd-type Fe$_2$Cr$_2$O$_5$ in Figure 8 has five non-equivalent cation sites (M1 – M5), four of which are

44   (Fe, Cr)O$_6$ octahedra with randomly distributed Fe and Cr, and the other a FeO$_6$ prism. These edge-shared

45   octahedra construct a zigzag framework, and the tunnels formed in this framework accommodate Fe. The Fe-O

46   distances of FeO$_6$ prism (M5 site) are 2.18-2.22 Å, and the average distance, 2.200 Å, is close to 2.18 Å by

47   summation of effective ionic radii of Fe^{2+} (0.78Å for six-fold coordination) and O^{2-} (1.40 Å) (Shannon, 1976).

48   The Fe$_2$Cr$_2$O$_5$ phase is the second compound with the mLd structure reported so far after the Mg$_2$Al$_2$O$_5$ phase.

49

50   3. Implications to FeCr$_2$O$_4$-rich high-pressure phases in the shocked Suizhou meteorite and to ultra-high

51   pressure chromitites in the Luobusa ophiolite complex.

52   The natural observation of CF-type and CT-type $FeCr_2O_4$-rich phases near the shock melt veins of the

53   Suizhou meteorite was first reported by Chen et al. (2003b). The CT-type $FeCr_2O_4$-rich phase was named xieite

54   (Chen et al., 2008). Our study indicates that at pressure above about 18 GPa CT-type $FeCr_2O_4$ and CF-type

55     $FeCr_2O_4$ are stable, but that CF-type $FeCr_2O_4$ is not quenched but changed into mCF-type which has a very

56   similar powder X-ray diffraction pattern to CF-type. Because of the very similar X-ray diffraction pattern of

57   mCF, it would be possible that Chen et al's CF-phase was not CF but mCF. Alternatively, minor components

58   such as Mg^{2+}, Al^{3+} etc. in the natural $FeCr_2O_4$-rich phase might stabilize the CF-type structure. Therefore, it is

59   desirable to directly analyze the structure of the natural CF-type $FeCr_2O_4$-rich phase in the meteorite. Figure 2

60   strongly suggests that the natural CF-type and CT-type $FeCr_2O_4$ rich-phases in the meteorite were formed above

61   about 18 GPa at temperatures lower and higher than 1300°C, respectively. It is interesting that the CT-type

62     $FeCr_2O_4$-rich phase was found within and in contact with the shock melt veins in the meteorite, and the CF-type

63     $FeCr_2O_4$-rich phase was found between the CT-type $FeCr_2O_4$-rich phase contacting with the shock melt veins

64   and $FeCr_2O_4$-rich chromite (Chen et al., 2003b, Chen et al., 2008). These observations are consistent with our

65   experimental results in Figure 2 in which the CT-type $FeCr_2O_4$ is stable at higher temperature than the CF-type.

66   The decomposition phases, $Fe_2Cr_2O_5$ mLd + Cr_2O_3 corundum, synthesized at 13-18 GPa in this study were not

67   observed between $FeCr_2O_4$-rich chromite and those of the CF-type and CT-type phases in the shocked meteorite.

68   The high-pressure polymorphs including CT-type $FeCr_2O_4$ rich-phase (xieite), CF-type $FeCr_2O_4$ rich-phase,

69   majorite garnet, Fe-bearing ringwoodite and $NaAlSi_3O_8$-rich lingunite were found in the meteorite (Xie et al.,

70   2011a, b). Considering the stability fields of these high-pressure phases (Kubo and Akaogi, 2000, Ito and

71   Takahashi, 1989, Yagi et al., 1994, Liu, 2006, Akaogi et al., 2010), it is inferred that these phases were

19

72   produced at pressure up to about 23 GPa and temperature up to liquidus temperature in various portions in the

73   meteorite during the shock event. Based on Figure 2, we suggest that the CF-type and CT-type $FeCr_2O_4$

74   rich-phases were formed in the portions of temperature below and above 1300 ^{o}C, respectively, at pressure

75   around 18-23 GPa.

76   Finally, we discuss the ultra-high pressure chromitites in the Luobusa ophiolite. High-pressure

77   minerals including diamond and coesite were found in the chromitites in the Luobusa ophiolite, Tibet (Yang et

78   al., 2007). Yang et al. (2007) suggested that coesite was formed by pseudomorphic replacement of stishovite

79   which was derived from the deep upper-mantle (>9 GPa). Furthermore, exsolution lamellaes of coesite and

80   clinopyroxene were found in chromite in the podiform chromitites of the Luobusa ophiolite (Yamamoto et al.,

81   2009). Yamamoto et al. (2009) suggested that these exsolution lamellaes in chromite were formed by the

82   process of the back-transformation from $FeCr_2O_4$-rich CF phase which could include other components such as

83   CaO and SiO_2 during mantle upwelling, and that ultrahigh-pressure chromitites in the Luobusa ophiolite were

84   originated from deep mantle at pressure above 12.5 GPa. We show that, in high-pressure phase relations of

85    $FeCr_2O_4$ in Figure 2, the stability field of $Fe_2Cr_2O_5$ mLd + Cr_2O_3 corundum exists at about 12-18 GPa between

86   those of $FeCr_2O_4$ spinel and CT-type or CF-type phase. However, the decomposed phases ($Fe_2Cr_2O_5$ + Cr_2O_3)

87   have not been reported in the natural chromitites in the Luobusa ophiolite. Based on our results, we suggest that

88   the chromitites have not undergone the mantle condition deeper than 12-16 GPa, because the decomposed

89   phases would have been likely preserved in the chromitites if the chromitites had really been subducted to the

90   deeper conditions.

91

20

Acknowledgements

Appendix

The synchrotron X-ray diffraction patterns of the whole 2θ range for modified $CaFe_2O_4$-type $FeCr_2O_4$, $CaTi_2O_4$-type $FeCr_2O_4$ and modified ludwigite-type $Fe_2Cr_2O_5$ are deposited as Figure 1(a), (b) and (c), respectively, at the MSA website.

References cited

Akaogi, M., Hamada, Y., Suzuki, T., Kobayashi, M., Okada, M. (1999) High-pressure transitions in the system $MgAl_2O_4$-$CaAl_2O_4$: a new hexagonal aluminous phase with implication for the lower mantle. Physics of the Earth and Planetary Interiors, 115, 67–77.

Akaogi, M., Haraguchi, M., Nakanishi, K., Ajiro, H., Kojitani, H. (2010) High-pressure phase relations in the system $CaAl_4Si_2O_{11}$-$NaAl_3Si_3O_{11}$ with implication for Na-rich CAS phase in shocked Martian meteorites, Earth and Planetary Science Letters, 289, 503-508.

21

12   Arai, S. (2010) Possible recycled origin for ultrahigh-pressure chromitites in ophiolite. Journal of Mineralogical

13   and Petrological Sciences, 105, 280-285, doi: 10.2465/jmps.100622a.

14   Arévalo-López, Á.M., Dos santos-García, A.J., Castillo-Martínez, E., Durán, A., Alario-Franco, M.Á. (2010)

15   Spinel to $CaFe_2O_4$ Transformation: Mechanism and Properties of β-$CdCr_2O_4$. Inorganic Chemistry, 49,

16   2827-2833, doi:10.1021/ic902228h.

17   Baerlocher, Ch., McCusker, L.B., Palatinus, L. (2007) Charge flipping combined with histogram matching to

18   solve complex crystal structures from powder diffraction data, Zeitschrift für Kristallographie, 222(2), 47-53.

19   Belokoneva, E.L., Shcherbakova, Y.K. (2003) Electron density in synthetic escolaite Cr_2O_3 with a corundum

20   structure and its relation to antiferromagnetic properties, Russian journal of inorganic chemistry, 48,

21   861-869.

22   Bertaut, E.F. and Blum, P. (1956) Détermination de la Structure Ti_2CaO_4 par la Méthode Self-Consistence

23   d'Approche Directe. Acta Crystallographyca, 9, 121-125.

24   Brown, I.D., Altermatt, D. (1985) Bond-valence parameters obtained from a systematic analysis of the

25   Inorganic Crystal Structure Database. Acta Crystallographica, B41, 244–247.

26   Chen, M., Shu, J., Xie, X., Mao, H.K. (2003a) Natural $CaTi_2O_4$-structure $FeCr_2O_4$ polymorph in the Suizhou

27   meteorite and its significance in mantle mineralogy. Geochimica et Cosmochimica Acta, 67, 3937-3942, doi:

28   10.1016/S0016-7037(03)00175-3.

29   Chen, M., Shu, J., Mao, H.K., Xie, X., Hemley, R.J. (2003b) Natural occurrence and synthesis of two new

30   postspinel polymorphs of chromite. PNAS, 100, 14651-14654, doi/10.1073/pnas.2136599100.

31   Chen, M., Shu, J., Mao, H.K. (2008) Xieite, a new mineral of high-pressure $FeCr_2O_4$ polymorph. Chinese

22

32   Science Bulletin, 53, 3341-3345, doi: 10.1007/s11434-008-0407-1.

33   Decker, B.F., Kasper, J.S. (1957) The structure of calcium ferrite. Acta Crystallographyca, 10, 332-337.

34   Dubrovinsky, L.S., Dubrovinskaia, N.A., Prokopenko, V.B., Le Bihan, T. (2002) Equation of state and crystal

35   structure of $NaAlSiO_4$ with calcium-ferrite type structure in the conditions of the lower mantle. High

36   Pressure Research, 22, 495-499.

37   Dunn, K.J., Bundy, F.P., (1978) Materials and techniques for pressure calibration by resistance-jump transitions

38   up to 500 kilobars. Review of Scientific Instruments, 49, 365-370.

39   Enomoto, A., Kojitani, H., Akaogi, M., Yusa, H. (2009) High-pressure transitons in $MgAl_2O_4$ and a new

40   high-pressure   phase   of $Mg_2Al_2O_5$.   Journal   of   Solid   State   Chemistry,   182,   389-395,

41   doi:10.1016/j.jssc.2008.11.015.

42   Fei, Y. and Bertka, C.M. (1999) Phase transitions in the Earth's mantle and mantle mineralogy. In: Fei, Y.,

43   Bertka, C.M., Mysen, B.O. (Eds.), Mantle Petrology: Field Observations and High Pressure Experimentation:

44   The Geochemistry Society, pp. 189–207.

45   Fei, Y., Orman, J. Van., Li, J., Western, W. Van., Sanloup, C., Minarik, W., Hirose, K., Komabayashi, T. (2004)

46   Experimentally determined post-spinel transformation boundary Mg_2SiO_4 using MgO as an internal pressure

47   standard   and   its   geophysical   implications.   Journal   of   Geophysical   Research,   109,   doi:

48   10.1029/2003JB002562.

49   Funamori, N., Jeanloz, R., Nguyen, J.H. Karner, A., Caldwell, W.A. (1998) High-pressure transforms in

50      $MgAl_2O_4$. Journal of Geophysical Research, 103, 20813-20818, doi: 101029/98JB01575.

51   Geisber, H.G., PenningtonW.T., Kolis, J.W. (2001) Redetermination of $CaMn_2O_4$. Acta Crystallographyca, C57,

52   329-330.

53   Hill P.M., Peiser, H.S., Rait, J.R. (1956) The crystal structure of calcium ferrite and β calcium chromite. Acta

54   Crystallographyca, 9, 981-986, doi:10.101107/S0365110X56002862.

55   Inaguma, Y., Sakurai, D., Aimi, A., Yoshida, M., Katsumata, Y., Mori, D., Yeon, J., Halasyamani, P.S. (2012)

56   Dielectric properties of a polar $ZnSnO_3$ with $LiNbO_3$-type structure. Journal of Solid State Chemistry, 195,

57   115-119.

58   Irifune, T., Naka, H., Sanehira, T., Inoue T., Funakoshi, K., (2002) In situ X-ray observations of phase

59   transitions in $MgAl_2O_4$ spinel to 40 GPa using multianvil apparatus with sintered diamond anvils. Physics

60   and Chemistry of Minerals, 29, 645-654.

61   Ishii, T., Kojitani, H., Akaogi, M., (2011) Post-spinel transitions in pyrolite and Mg_2SiO_4 and

62   akimotoite-perovskite transition in $MgSiO_3$: Precise comparison by high-pressure high-temperature

63   experiments with multi-sample cell technique. Earth and Planetary Science Letters, 309, 185-197, doi:

64   10.1016/j.epsl.2011.06.023.

65   Ishii, T., Kojitani, H., Akaogi, M., (2012) High-pressure phase transitions and subduction behavior of

66   continental crust a pressure-temperature conditions up to the upper part of the lower mantle. Earth and

67   Planetary Science Letters, 357-358, 31-41, doi: 10.1016/j.epsl.2012.09.019.

68   Ito, E., 2007. Theory and Practice – Multianvil cells and high-pressure experimental methods, in: G. Schubert,

69   B. Romanowicz, A. Dziewonski (Eds.), Mineral Physics, 2, pp. 197-230. Treatise on Geophysics, Elsevier,

70   Amsterdam.

71   Ito, E. and Takahashi, E. (1989) Post-spinel transformation in the system Mg_2SiO_4-Fe_2SiO_4 and some

72   geophysical implications. Journal of Geophysical Research, 94, 10637-10646.

73   Izumi, F., and Momma, K. (2007) Three-dimensional visualization in powder diffraction. Solid State

74   Phenomena, 130, 15-20.

75   Kojitani, H., Enomoto, A., Tsukamoto, S., Akaogi, M., Miura, H., Yusa, H. (2010) High-pressure

76   high-temperature phase relations in $MgAl_2O_4$. Journal of physics: Conference Series, 215, 012098,

77   doi:10.1088/1742-6596/215/1/012098.

78   Kosiner, K. and Rea, J.R. (1974) Crystal structure of ferrous phosphate, $Fe_3(PO_4)_2$, Inorganic Chemistry, 13,

79   2876-2880, doi: 10.1021/ic50142a021.

80   Kubo, A. and Akaogi, M. (2000) Post-garnet transitions in the system $Mg_4Si_4O_{12}$-$Mg_3Al_2Si_3O_{12}$ up to 28 GPa:

81   phase relations of garnet, ilmenite and perovskite. Earth and Planetary Interiors, 121, 85-102.

82   Kyono, A., Gramsch S.A., Yamanaka, T., Ikuta, D., Ahart, M., Mysen, B.O., Mao, H.K. Hemley, R.J. (2012)

83   The influence of the Jahn-Teller effect at Fe2+ on the structure of chromite at high pressure. Physics and

84   Chemistry of Minerals, 39, 131-141, doi:10.1007/s00269-011-0468-6.

85   Larson, A.C. and Von Dreele, R.B. (2000) General structure analysis system (GSAS). Los Alamos National

86   Laboratory Report, LAUR, 86–748.

87   Lavina, B., Dera, P., Kim, E., Meng, Y., Downs, R.T., Weck, P.F., Sutton, S.R., Zhao, Y. (2011) Discovery of the

88   recoverable high-pressure iron oxide Fe_4O_5. PNAS, 108, 17281-17275, doi/10.1073/pnas.1107573108.

89   Le Bail, A., Duroy, H., Fourquet, J. L., (1988) Ab-initio structure determination of $LiSbWO_6$ by X-ray powder

90   diffraction, Materials Research Bulletin, 23, 447.

91   Lenaz, D., Skogby, H., Princivalle, F., Halenius, U. (2004) Structural changes and valence states in the $MgCr_2$

92   O_4-$FeCr_2O_4$ solid   solution   series.   Physics   and   Chemistry   of   Minerals,   31,   633-642,   doi:

93   10.1007/s00269-004-0420-0.

94   Liu, X. (2006) Phase relations in the system $KAlSi_3O_8$-$NaAlSi_3O_8$ at high pressure – high temperature

95   conditions and their implications for the petrogenesis of lingunite. Earth and Planetary Science Letters, 246,

96   317-325.

97   Louër, D. and Boultif, A. (2007) Powder pattern indexing and the dichotomy algorithm. Zeitschrift für

98   Kristallographie Supplements, 26, 191-196, doi: 10.1524/zksu.2007.2007.suppl_26.191.

99   McCammon, C. (1993) Composition limits of Fe_xO and the earth's lower mantle. Science, 261, 923-925.

00   Momma, K. and Izumi, F. (2008) VESTA: a three-dimensional visualization system for electronic and structural

01   analysis. Journal of Applied Crystallography, 41, 653-658.

02   Morishima, H., Kato, T., Suto, M., Ohtani, E., Urakawa, U., Shimomura, O., Kikegawa, T. (1994) The phase

03   boundary between alpha-Mg_2SiO_4 and beta-Mg_2SiO_4 determined by in-situ x-Ray observation. Science, 265,

04   1202-1203.

05   Nespolo, M., Ferraris, G., Hoppe, R. (2001) Charge distribution analysis of ceramic materials. Journal of

06   Ceramic Processing Research, 2, 38-44.

07   Ohtani, E., Hirao, N., Kondo, T., Ito, M., Kikegawa, T. (2005) Iron-water reaction at high-pressure and

08   temperature, and hydrogen transport into the core. Physics and Chemistry of Minerals, 32, 77-82, doi:

09   10.1007/s00269-004-0443-6.

10   Ono, S., Kikegawa, T., Ohishi, Y. (2006) The stability and compressibility of $MgAl_2O_4$ high-pressure

11   polymorphs. Physics and Chemistry of Minerals, 33, 200-206, doi: 10.1007/s00269-006-0068-z.

12   Palatinus, L. and Chapuis, G. (2007) Superflip - a computer program for the solution of crystal structures by

13   charge flipping in arbitrary dimensions. Journal of Applied Crystallography, 40, 786-790.

14   Palatinus, L., Prathapa, S. J., van Smaalen, S. (2012): EDMA: a computer program for topological analysis of

15   discrete electron densities. Journal of Applied Crystallography, 45, 575-580.

16   Rabin, H. and Tang, C.L. (1975) Physics; Nonlinear Optical Susceptibilities; Nonlinear Optical Process;

17   Parametric; Raman; Spectroscopy. Quantum Electronics, 1.

18   Ringwood, A.E. (1975) Composition and Petrology of the Earth's Mantle. McGraw-Hill, New York, NY,

19   618pp.

20   Rogge, M.P., Caldwell, J.H., Ingram, D.R., Green, C.E., Geselbracht, M.J., andSiegrist, T. (1998) A new

21   synthetic route to peseudo-brookite-type $CaTi_2O_4$. Journal of Solid State Chemistry, 141, 338–342.

22   Sanehira, T., Irifune, T., Shinmei, T., Ohfuji, H., Brunet, F., Funakoshi, K.-I. (2008) Density profiles of pyrolite

23   and MORB compositions across the 660-km seismic discontinuity. High Pressure Research, 28, 335-349,

24   doi:10.1080/08957950802251357.

25   Shannon, R.D. (1976) Revised effective ionic radii and systematic studies of interatomic distances in halides

26   and chalcogenides. Acta Crystallographica, A32, 751-767.

27   Speziale, S., Zha, C.S., Duffy, T.S., Hemley, R.J., Mao, H.K. (2001) Quasi-hydrostatic compression of

28   magnesium oxide to 52 GPa: implications for the pressure-volume-temperature equation of state. Journal of

29   Geophysical Research, 106, 515-528.

30   Suzuki, A., Ohtani, E., Morishima, H., Kubo, T., Kanbe, Y., Kondo, T. (2000). In situ determination of the phase

31   boundary between wadsleyite and ringwoodite in Mg_2SiO_4, Geophysical Research Letters, 27, 803-806.

27

32   Toby, B.H. (2001) EXPGUI, a graphical user interface for GSAS. Journal of Applied Crystallography, 34,

33   210–213.

34   Xie, X., Chen, M., Wang, C.Y. (2011a) Occurrence and mineral chemistry of chromite and xieite in the Suizhou

35   L6 chondrite. Science China Earth Science, 54, 998-1010, doi: 10.1007/s11430-011-4199-9.

36   Xie, X., Sun, Z., Chen, M. (2011b) The distinct morphological and petrological features of shock melt veins in

37   the Suizhou L6 chondrite. Meteoritics and Planetary Science, 46, 459-469, doi:

38   10.1111/j.1945-5100.2100.01168.x.

39   Yagi, A., Suzuki, T., Akaogi, M. (1994) High pressure transitions in the system $KAlSi_3O_8$-$NaAlSi_3O_8$. Physics

40   and Chemistry of Minerals, 21, 12-17.

41   Yamamoto, S., Kojima, T., Hirose, K., Maruyama, S. (2009) Coesite and clinopyroxene exsolution lamella in

42   chromites: *In-situ* ultrahigh-pressure evidence from podiform chromitites in the Luobusa ophiolite, southern

43   Tibet. Lithos, 109, 314-322.

44   Yamanaka, T., Uchida, A., Nakamoto, Y. (2009) Structural transition of post-spinel phases $CaMn_2O_4$, $CaFe_2O_4$

45   and $CaTi_2O_4$ under high-pressures up to 80 GPa. American Mineralogist, 93, 1874-1881.

46   Yang, J.S., Dobrzhinetskaya, L., Bai, W.J., Fang, Q.S., Robinson, P.T., Zhang, J., Green, H.W. (2007)

47   Diamond– and coesite-bearing chromitites from the Luobusa ophiolite, Tibet. Geology, 35, 875-878, doi:

48   10.1130/G23766A

49

28

50   **Figure captions**

51

52   **Figure 1.** Synchrotron X-ray diffraction pattern of $FeCr_2O_4$ phase synthesized at 25 GP and 1000^oC. The

53   pattern was taken at ambeint conditions. Miller indices are based on the unit cell of modified $CaFe_2O_4$-type

54    $FeCr_2O_4$ in Table 2. Es represents diffraction peaks of Cr_2O_3 escolaite (upper figure). The blue pattern

55   represents simulated pattern of $CaFe_2O_4$-type $FeCr_2O_4$ (lower figure). Note that intensities of 202, 104, 211,401

56   and 113 peaks in the observed XRD pattern are different from the coresponding peaks in the simulated pattern.

57

58   **Figure 2.** Phase relations of $FeCr_2O_4$ at high pressure and high temperature. Solid circle, Sp; half closed circle,

59   Sp + mLd + Es; solid square, mLd + Es; half closed square, mLd + Es + CT; solid triangle, CF; solid inverse

60   triangle, CT; half closed inverse triangle, CF + CT. Solid lines represent phase boundaries. Sp, spinel-type

61    $FeCr_2O_4$; mLd, modified ludwigite-type $Fe_2Cr_2O_5$; Es, Cr_2O_3 eskolaite; CF, $CaFe_2O_4$-type $FeCr_2O_4$; CT,

62    $CaTi_2O_4$-type $FeCr_2O_4$.

63

64   **Figure 3.** (a) *In-situ* X-ray diffraction profiles of $FeCr_2O_4$ as a function of pressure and temperature. Small red

65   circles indicate diffraction peaks whose intensities are different from those of $CaFe_2O_4$-type $FeCr_2O_4$. c-Sp:

66   cubic spinel, t-Sp: tetragonal spinel. (b) *In-situ* X-ray diffraction pattern of $CaFe_2O_4$-type $FeCr_2O_4$ with small

67   amounts of γ-FeH_x and FeO (upper figure). Simulated pattern of $CaFe_2O_4$-type $FeCr_2O_4$ (lower figure). Both

68   patterns are at 16.5 GPa and 27 ^oC. (c) Compression curve of $CaFe_2O_4$-type $FeCr_2O_4$ up to 25 GPa at 27 ^oC.

69   The solid line represents the Birch-Murnaghan fitting curve.

29

70

71   **Figure 4.** Electron diffraction patterns of (a) $hk0$ plane, (b) $h0l$ plane, and (c) $0kl$ plane of the recovered sample

72   (Run no. 40). The electron diffraction patterns were taken from different grains of the same run product.

73

74   **Figure 5.** Synchrotron X-ray diffraction patterns of (a) modified $CaFe_2O_4$-type $FeCr_2O_4$, (b) $CaTi_2O_4$-type

75    $FeCr_2O_4$ and (c) modified ludwigite-type $Fe_2Cr_2O_5$ at ambient conditions. The diffraction patterns in (a), (b)

76   and (c) show those in 2θ ranges below 35, 45 and 40°, respectively. The diffraction patterns in the whole 2θ

77   range up to 75° (deposited in Appendix) were used for Rietveld refinements. Data points and solid lines show

78   the observed and the calculated profiles, respectively, and the difference between them is shown at the bottom.

79   Bragg peak positions are marked by small ticks. These lines are for main phases, Cr_2O_3 eskolaite and Re from

80   top to bottom. The refined crystal structure is shown with each profile.

81

82   **Figure 6.** (a) and (b) Crystal structure of modified $CaFe_2O_4$-type $FeCr_2O_4$. (c) Coordination environments of Fe

83   and Cr. (d) Fe-O distances in the coordination environment of Fe.

84

85   **Figure 7.** (a) and (b) Crystal structure of $CaTi_2O_4$-type $FeCr_2O_4$. (c) Coordination environments of Fe and Cr.

86   (d) Fe-O distances in the coordination environment of Fe.

87

88   **Figure 8.** (a) and (b) Crystal structure of modified ludwigite-type $Fe_2Cr_2O_5$. (c) Coordination environments of

89   Fe and Cr. See Table 3 for site occupancies of Fe and Cr in M1-M5 sites. (d) Fe-O distances in M5 site.

90   Table 1

91   Results of high-pressure high-temperature quench experiments

Run no.	Pressure	Temperature	Duration	[†]Phases
	(GPa)	(°C)	(min)	
36	15.9	800	180	Sp
35	17.6	800	180	mCF
34	19.8	800	180	mCF
32	25.0	800	180	mCF
7	14.7	1000	120	Sp
12	15.9	1000	120	mLd+Es
14	16.5	1000	120	mLd+Es
22	17.6	1000	120	mCF
25	19.8	1000	120	mCF
40	25.0	1000	120	mCF
37	28.0	1000	120	mCF
39	15.9	1100	120	mLd+Es
38	28.0	1100	120	mCF
19	13.5	1200	120	Sp
18	14.7	1200	120	mLd+Es
10	17.6	1200	120	mLd+Es

31

10	24	18.6	1200	120	mCF
11	17	22.8	1200	120	mCF
12	23	25.0	1200	120	mCF
13	26	28.0	1200	120	mCF
14	27	22.8	1300	60	mCF
15	30	27.1	1300	60	mCF
16	31	28.0	1300	60	mCF+CT
17	13	13.0	1400	60	Sp
18	5	13.9	1400	60	Sp+mLd+Es
19	15	14.7	1400	60	mLd+Es
20	16	17.6	1400	60	mLd+Es
21	20	18.6	1400	60	mLd+Es+CT
22	28	19.8	1400	60	CT+mLd(tr)+Es(tr)
23	33	28.0	1400	60	CT
24	1	19.8	1500	60	CT
25	11	11.7	1600	60	Sp
26	8	13.0	1600	60	mLd+Es
27	4	14.7	1600	60	mLd+Es
28	9	15.9	1600	60	mLd+Es
29	6	16.6	1600	60	CT

32

| 30 | 2 | 23.0 | 1600 | 60 | CT |

31 [†]Phases in the recovered samples. A small amount of metallic iron in the run products derived from the starting

32 material, the mixture of $FeCr_2O_4$ spinel + 5 wt% Fe, is not listed.

33 Abbreviations: Sp, spinel-type $FeCr_2O_4$; mLd, modified ludwigite-type $Fe_2Cr_2O_5$; Es, Cr_2O_3 corundum; mCF,

34 modified $CaFe_2O_4$-type $FeCr_2O_4$; CT, $CaTi_2O_4$-type $FeCr_2O_4$; tr, trace.

35

36

37

38

39

40

41

42

43

44

45

46

47

48

49

50   Table 2

51   Lattice parameters of modified $CaFe_2O_4$(mCF)-type $FeCr_2O_4$, $CaTi_2O_4$(CT)-type $FeCr_2O_4$ and modified

52   ludwigite(mLd)-type $Fe_2Cr_2O_5$.

Phase	mCF-type $FeCr_2O_4$	CT-type $FeCr_2O_4$	mLd-type $Fe_2Cr_2O_5$
Space group	*Pnma* (no. 62)	*Cmcm* (no. 63)	*Pbam* (no. 55)
a (Å)	9.0633(3)	2.8845(1)	9.6642(2)
b (Å)	2.9579(1)	9.5207(2)	12.5000(3)
c (Å)	10.6391(3)	9.7532(2)	2.9023(1)
V (Å^3)	285.22(1)	267.84(1)	350.59(1)
Z	4	4	4
V_m (cm^3/mol)	42.941(2)	40.323(2)	52.781(2)
D (g/cm^3)	5.213(1)	5.553(1)	5.604(1)

53 ... 69 (line numbers)

34

70   Table 3

71   Structure parameters of modified CaFe$_2$O$_4$(mCF)-type FeCr$_2$O$_4$, CaTi$_2$O$_4$(CT)-type FeCr$_2$O$_4$ and modified

72   ludwigite(mLd)-type Fe$_2$Cr$_2$O$_5$.

Atom	Wyckoff site	g (Fe)	g (Cr)	x	y	z	B_{iso} (Å^2)
mCF-type FeCr$_2$O$_4$							
Fe	4c	1.0	0.0	0.2560(2)	0.25	0.3300(2)	1.72(4)
Cr1	4c	0.0	1.0	0.0511(2)	0.25	0.6164(2)	0.50(3)
Cr2	4c	0.0	1.0	0.0904(2)	0.25	0.0974(2)	0.42(3)
O1	4c	-	-	0.3083(6)	0.25	0.1526(6)	0.84(6)
O2	4c	-	-	0.3895(6)	0.25	0.4759(6)	0.84(6)
O3	4c	-	-	0.4481(6)	0.25	0.7160(5)	0.84(6)
O4	4c	-	-	0.0803(6)	0.25	0.4323(6)	0.84(6)
CT-type FeCr$_2$O$_4$							
Fe	4c	1.0	0.0	0	0.1128(2)	0.25	1.76(4)
Cr	8f	0.0	1.0	0	0.3686(2)	0.0714(1)	0.25(2)
O1	4b	-	-	0	0	0	0.48(10)
O2	4c	-	-	0	0.4656(6)	0.25	0.65(11)
O3	8f	-	-	0	0.2640(4)	0.6109(3)	0.60(9)

89

35

90 mLd-type $Fe_2Cr_2O_5$

91	M1	2a	0.3	0.7	0	0	0	0.51(4)
92	M2	2d	0.8	0.2	0	0.5	0.5	0.43(4)
93	M3	4g	0.35	0.65	0.0221(2)	0.2824(1)	0	0.72(3)
94	M4	4h	0.1	0.9	0.2730(1)	0.3827(1)	0.5	0.13(3)
95	M5	4g	1.0	0.0	0.2432(2)	0.1306(2)	0	1.64(4)
96	O1	4h	-	-	0.1423(6)	0.0237(5)	0.5	0.68(4)
97	O2	4g	-	-	0.4115(5)	0.3510(5)	0	0.68(4)
98	O3	4h	-	-	0.4103(5)	0.1424(5)	0.5	0.68(4)
99	O4	4g	-	-	0.1373(6)	0.4296(5)	0	0.68(4)
00	O5	4h	-	-	0.1598(6)	0.2488(4)	0.5	0.68(4)

01 The reliability factors and goodness-of-fit indicator for the mCF.

02 $R_{wp} = 5.910\%$, $S = 0.9867$

03 mCF-type $FeCr_2O_4$: $R_B = 2.873\%$, $R_F = 1.512\%$

04 Corundum-type Cr_2O_3: $R_B = 4.245\%$, $R_F = 2.447\%$

05 The reliability factors and goodness-of-fit indicator for the CT.

06 $R_{wp} = 6.380\%$, $S = 1.0663$

07 CT-type $FeCr_2O_4$: $R_B = 1.969\%$, $R_F = 2.036\%$

08 Corundum-type Cr_2O_3: $R_B = 3.006\%$, $R_F = 2.773\%$

09 The reliability factors and goodness-of-fit indicator for the mLd.

10   $R_{wp} = 3.905\%$, $S = 0.6443$

11   mLd-type $Fe_2Cr_2O_5$: $R_B = 1.247\%$, $R_F = 0.935\%$

12   Corundum-type Cr_2O_3: $R_B = 2.420\%$, $R_F = 2.040\%$

13   Re: $R_B = 0.826\%$, $R_F = 0.532\%$

14   $$R_{wp} = \left\{ \frac{\sum_i w_i [y_i - f_i(x)]^2}{\sum_i w_i y_i^2} \right\}^{1/2}, \quad R_B = \frac{\sum_K |I_0(h_K) - I(h_K)|}{\sum_K I_0(h_K)}, \quad R_F = \frac{\sum_K ||F_0(h_K)| - |F(h_K)||}{\sum_K |F_0(h_K)|}, \quad S = \left\{ \frac{\sum_i w_i [y_i - f_i(x)]^2}{N - P} \right\}^{1/2}$$

15   where y_i, w_i and $f_i(x)$ are the observed intensity at step i, the statistical weight and calculated intensity, $I_0(h_K)$,

16   $I(h_K)$, $F_0(h_K)$ and $F(h_K)$ are the observed and calculated intensity and structure factor for reflection K, N and P

17   are number of all data points and refined parameter, respectively.

18

19

20

21

22

23

24

25

26

27

28

29

37

30   Table 4

31   Interatomic distances and angles in the structures of modified $CaFe_2O_4$(mCF)-type $FeCr_2O_4$, $CaTi_2O_4$(CT)-type

32    $FeCr_2O_4$ and modified ludwigite(mLd)-type $Fe_2Cr_2O_5$.

mCF-type $FeCr_2O_4$		CT-type $FeCr_2O_4$		mLd-type $Fe_2Cr_2O_5$	
Bond length (Å)		Bond length (Å)		Bond length (Å)	
Fe−O1	1.945(6)	Fe−O1 × 2	2.6644(7)	M1−O1 × 4	2.021(4)
Fe−O2	1.968(6)	Fe−O2 × 2	2.011(5)	M1−O2 × 2	2.049(6)
Fe−O3[i] × 2	2.661(5)	Fe−O3 × 4	2.301(3)	Average	2.030
Fe−O4	1.928(5)	Average	2.319	n_c	5.99
Average	2.233	n_c	4.87	BVS	2.64
n_c	3.01	BVS	1.97	M2−O3 × 2	1.980(6)
BVS	1.85	Cr1−O1[i] × 2	2.0323(9)	M2−O4 × 4	2.155(4)
Cr1−O1[i] × 2	1.991(4)	Cr1−O2	1.972(3)	Average	2.097
Cr1−O3[ii]	2.013(6)	Cr1−O3 × 2	1.955(3)	n_c	5.55
Cr1−O4[iii] × 2	1.968(4)	Cr1−O3	2.038(3)	BVS	2.30
Cr1−O4	1.977(6)	Average	1.997	M3−O2	1.980(6)
Average	1.985	n_c	5.92	M3−O3 × 2	2.039(4)
n_c	5.99	BVS	2.88	M3−O4	2.151(6)
BVS	2.97	Bond angles (º)		M3−O5 × 2	2.013(4)
Cr2−O1	2.060(6)	Cr1[iv]−O1−Cr1[iv]	90.42(5)	Average	2.039

38

50	$Cr2-O2^{ii}$	1.981(5)	$Cr1^{v}-O1^{vi}-Cr^{v}$	89.58(5)	n_c	5.85
51	$Cr2-O2^{i} \times 2$	1.973(4)	$Cr1^{vii}-O3^{vi}-Cr1^{vii}$	95.1(2)	BVS	2.61
52	$Cr2-O3^{i} \times 2$	1.975(4)	$Cr1^{vii}-O3i^{vii}-Cr1^{viii}$	98.2(1)	$M4-O1$	1.943(6)
53	Average	1.990	$Cr1^{vii}-O2^{vi}-Cr1^{viii}$	124.1(3)	$M4-O2 \times 2$	2.014(4)
54	n_c	5.95	$O3^{v}-Cr1^{vi}-O1^{vii}$	171.3(1)	$M4-O4 \times 2$	2.042(4)
55	BVS	2.94	$O2^{vi}-Cr1^{vi}-O3^{viii}$	178.7(2)	$M4-O5$	2.000(6)
56	Bond angles (º)				Average	2.009
57	$Cr1^{i}-O1-Cr1^{i}$	96.0(3)			n_c	5.93
58	$Cr1^{iii}-O4-Cr1^{iii}$	97.4(3)			BVS	2.80
59	$Cr1^{iii}-O4-Cr1$	100.3(2)			$M5-O1 \times 2$	2.201(5)
60	$Cr2^{i}-O2-Cr2^{i}$	97.1(2)			$M5-O3 \times 2$	2.176(4)
61	$Cr2^{i}-O2-Cr2^{ii}$	100.0(2)			$M5-O5 \times 2$	2.223(4)
62	$Cr2^{i}-O3-Cr2^{i}$	97.0(2)			Average	2.200
63	$Cr1^{i}-O1-Cr2$	124.0 (2)			n_c	5.98
64	$Cr2^{i}-O3-Cr1^{ii}$	130.4(1)			BVS	1.71
65	$O4-Cr1-O3^{ii}$	160.1(3)			Bond angles (º)	
66	$O4^{iii}-Cr1-O1^{i}$	175.5(3)			$O1-M1-O1^{iii}$	89.1(3)
67	$O2^{ii}-Cr2-O1$	95.2(2)			$O1-M1-O2^{ix}$	98.8(2)
68	$O2^{ii}-Cr2-O3^{i}$	173.4(3)			$O4-M2-O4^{iii}$	173.4(3)
69					$O3^{ix}-M2-O4^{iii}$	84.2(2)

39

70	$O5^{vi}$−M3−$O3^{ix}$	163.7(3)
71	$O2^{ix}$−M3−O4	178.3(3)
72	O2−M4−$O4^{vi}$	174.8(3)
73	$O1^{x}$−M4−O5	171.0(3)
74	$M3^{ix}$−$O2^{vi}$−$M1^{x}$	122.2(3)
75	M1−O1−$M1^{vi}$	90.9(3)
76	$M4^{vi}$−O2−M1	95.9(3)
77	$M4^{x}$−O1−$M1^{vi}$	98.2(3)
78	M2−O4−$M2^{vi}$	84.9(2)
79	M3−O4−$M2^{vi}$	92.0(2)
80	M2−O3−$M3^{ix}$	100.4(2)
81	M4−O4−M2	91.98(4)
82	$M3^{ix}$−O3−$M3^{ix}$	90.7(3)
83	M3−O5−$M3^{iv}$	92.1(3)
84	$M4^{vi}$−O4−M3	95.2(2)
85	M4−O5−M3	100.7(2)
86	$M3^{ix}$−O2−M4	121.5(2)
87	M4−O2−$M4^{vi}$	92.8(3)
88	M4−O4−$M4^{vi}$	90.3(3)

89 Symmetry codes: (i) 1/2−x, −y, 1/2+z. (ii) 1/2+x, y, 1/2−z. (iii) −x, −y, −z. (iv) 1/2−x, 1/2−y, −z. (v) 1/2−x,

40

90   1/2−y, 1/2+z. (vi) x, y, z. (vii) 1/2+x, 1/2+y, z. (viii) x, y, 1/2−z. (ix) 1/2+x, 1/2−y, z. (x) 1/2−x, 1/2+y, −z.

91   n_c: effective coordination number
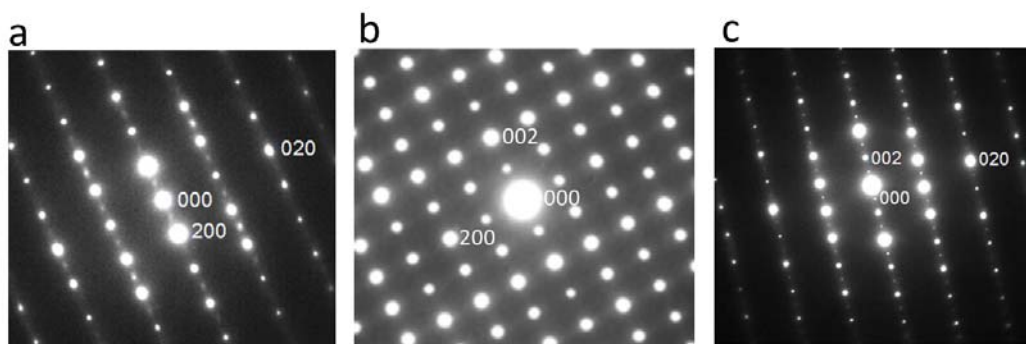
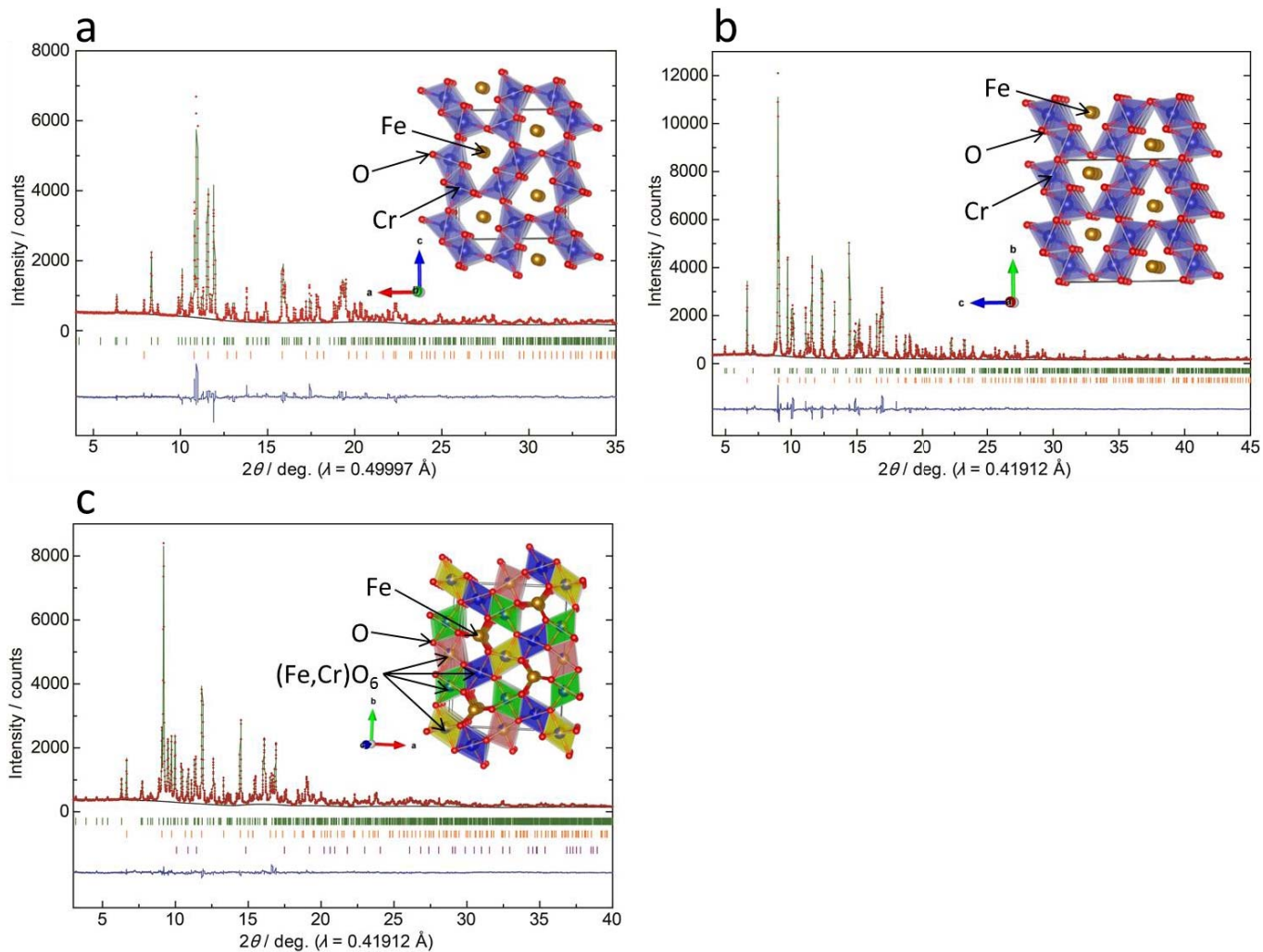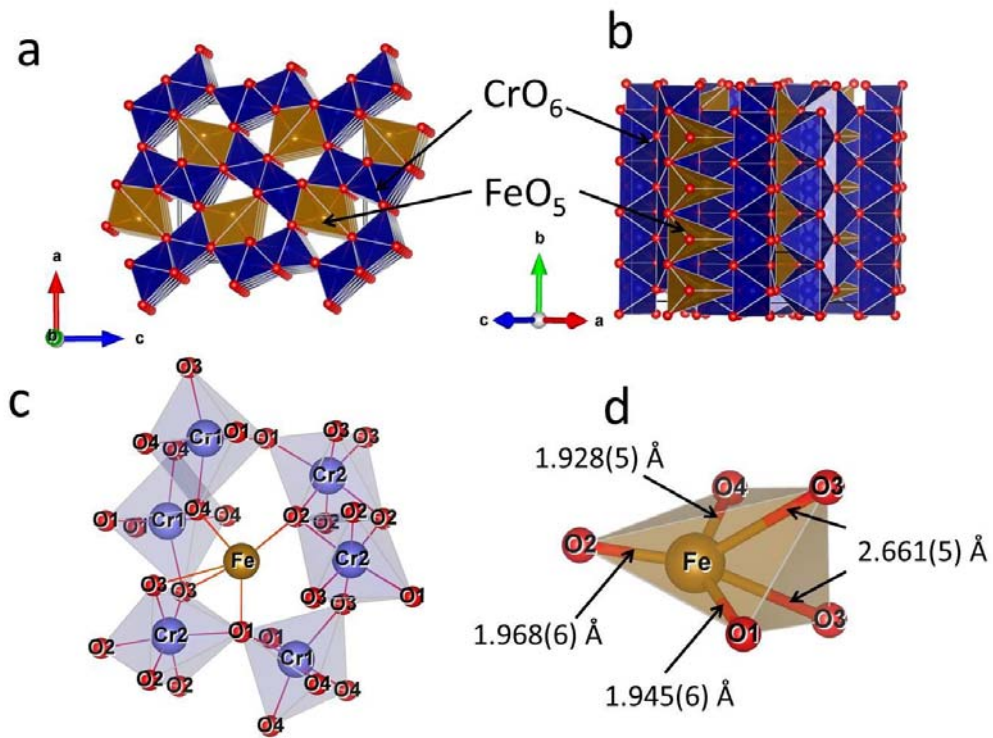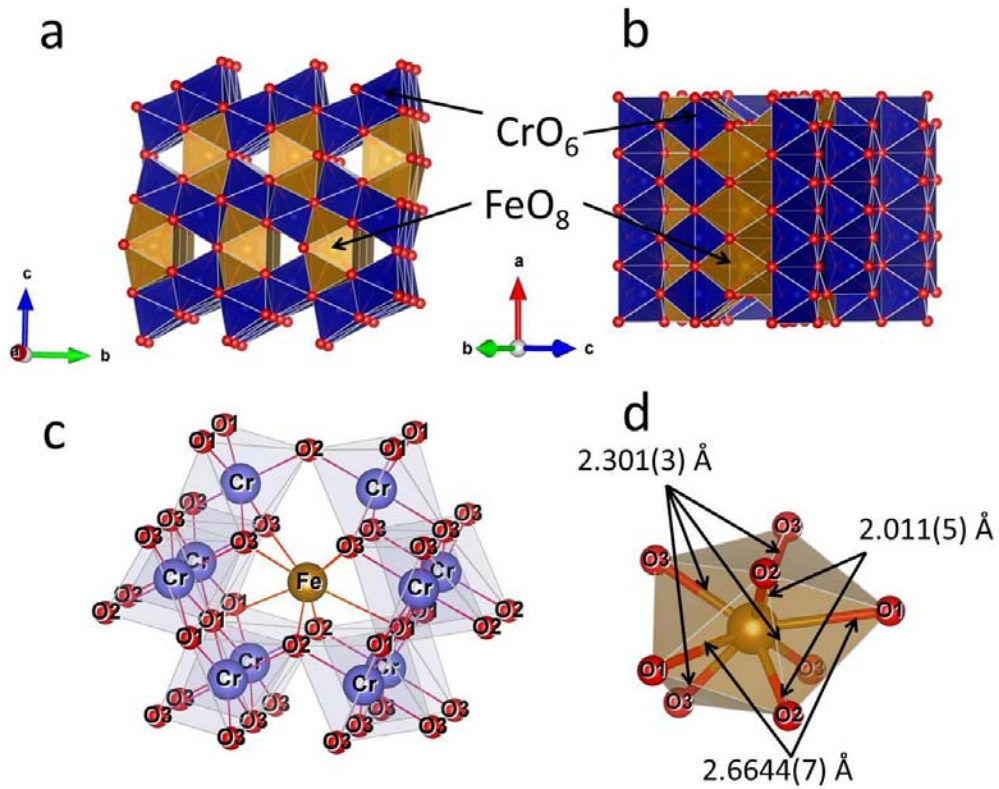92   BVS: bond valence sum value
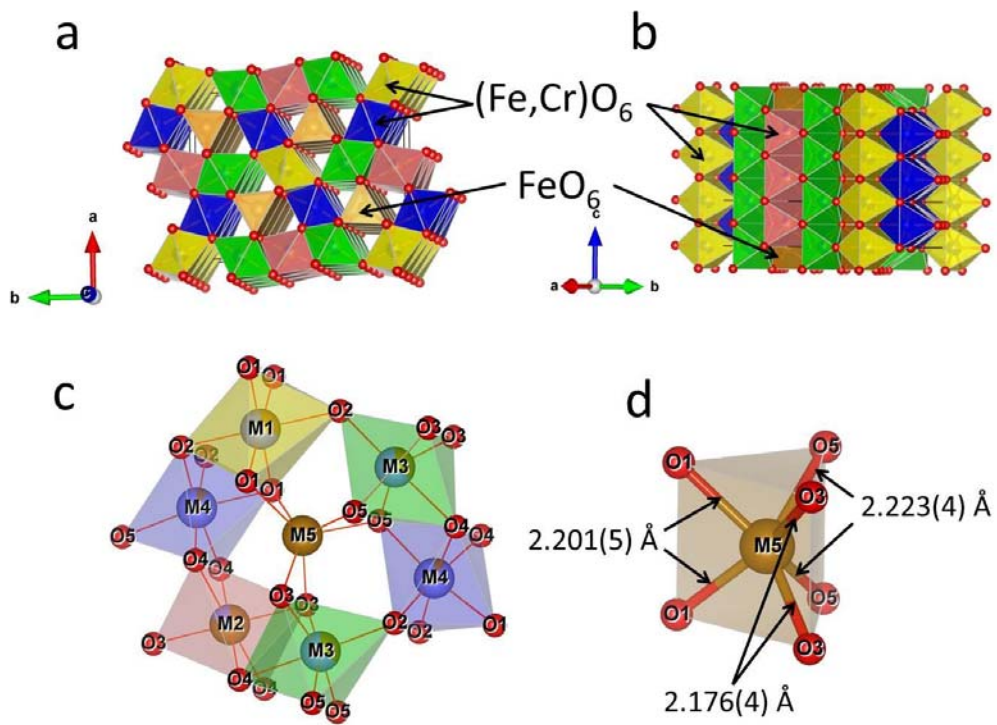
93
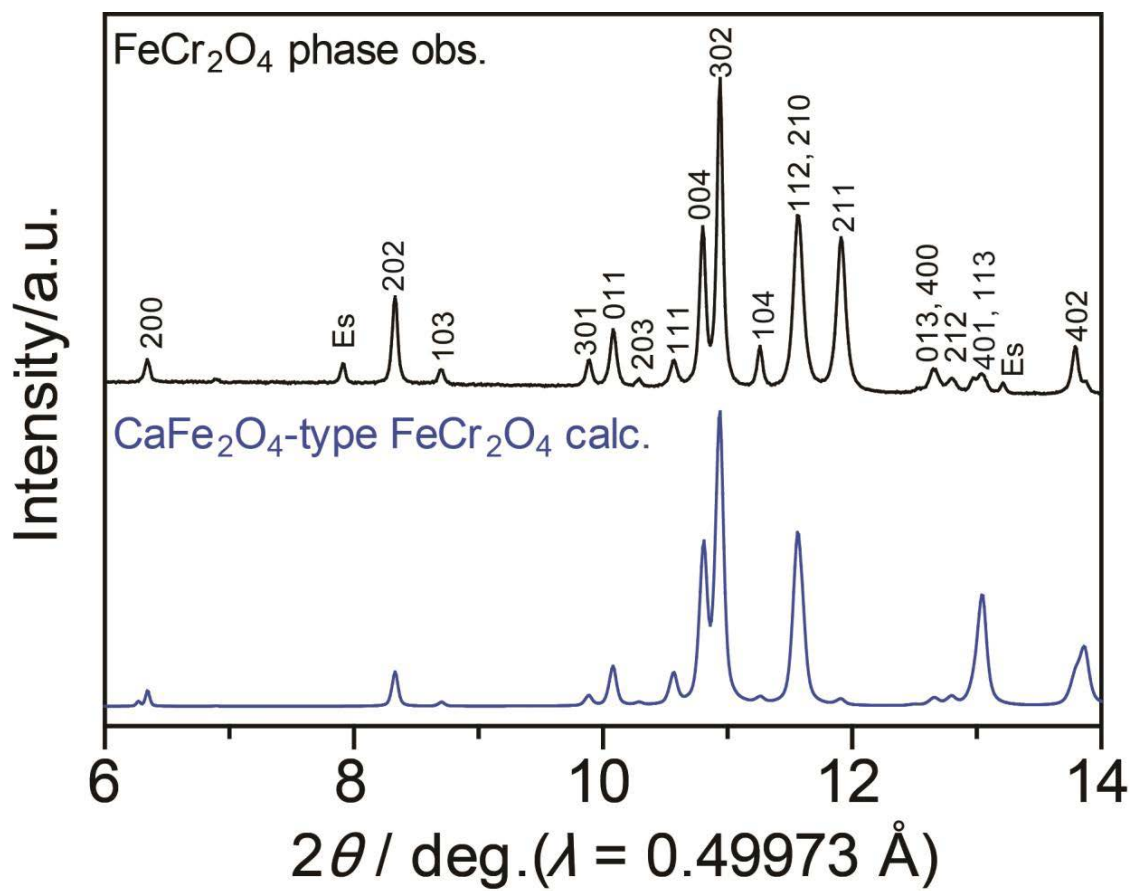
Figure 1.
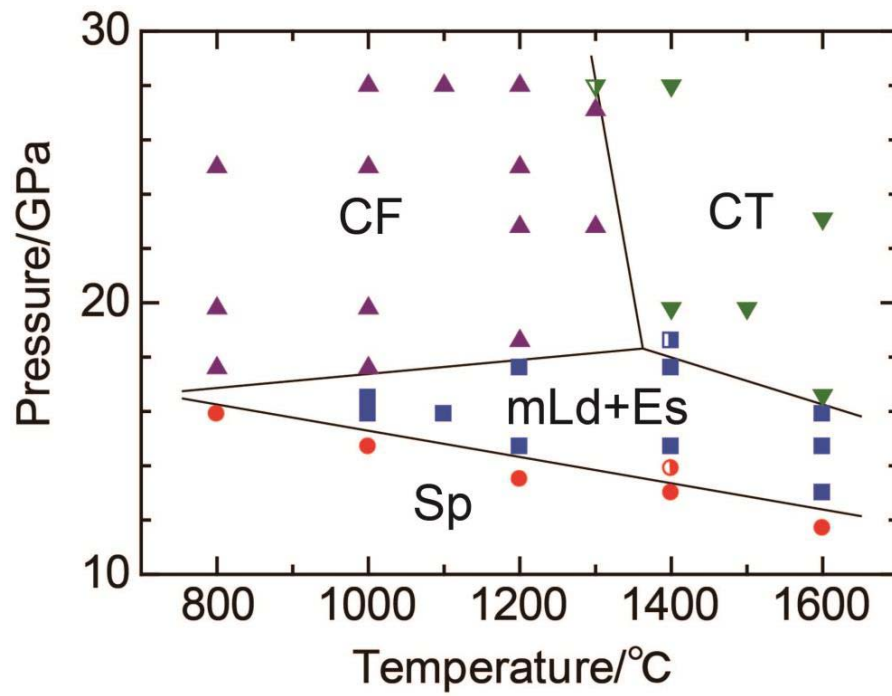
Figure 2
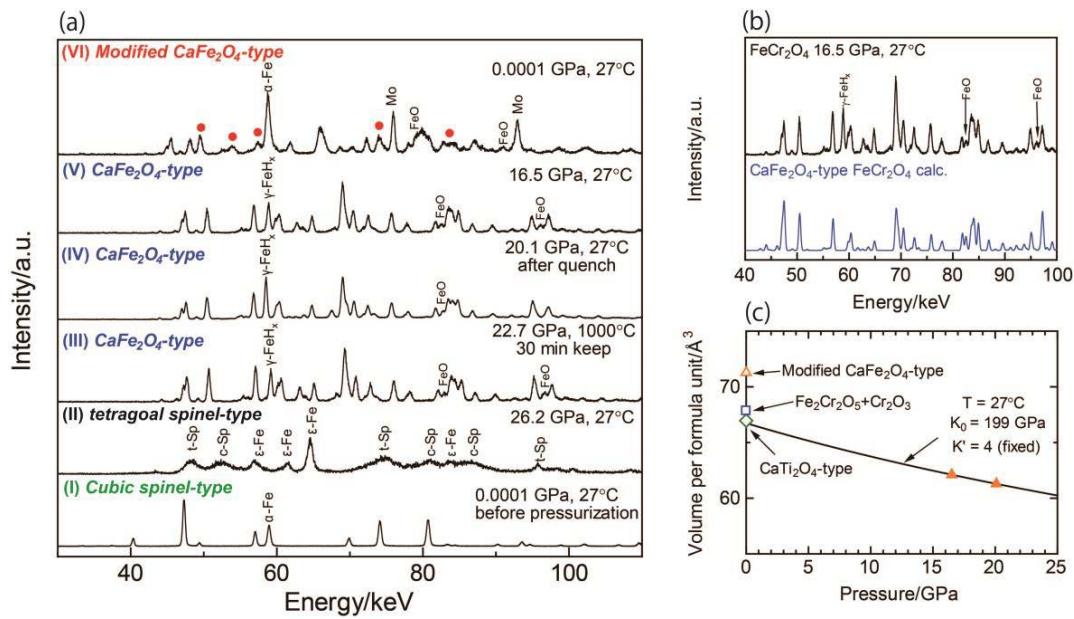
Figure 3.

Figure 4.

Figure 5.

Figure 6.

Figure 7.

Figure 8.